Computational Heat Transfer with Spectral Graph Theory: Quantitative Verification

Kevin D. Cole¹, M. Reza Yavari, Prahalad K. Rao Mechanical and Materials Engineering, University of Nebraska–Lincoln, Lincoln, NE 68588-0526

Revision submitted to the Int. J. Thermal Sciences, March 11, 2020

Abstract

The objective of this paper is to quantify the precision of a novel approach for computational heat transfer modeling based on spectral graph theory. Two benchmark heat transfer problems with planar boundaries, for which exact analytical solutions are available, are used to determine the precision of temperature predictions obtained from spectral graph, finite difference (one-dimensional), and finite element (three-dimensional) methods. These studies show that the spectral graph approach captures the temperature trends in the benchmark case studies with error in the range of 2% to 10% depending on the location in the body. These verification studies also provide an approach to calibrate the numerical parameters in the new method. The spectral graph approach is applied for predicting the thermal history of a complex three-dimensional additive manufactured (3D printed) part. The temperature trends in a 50-layer part are computed 2.3 times faster than a commercial finite-element software package, and the results differ by less than 7.5%. Further improvements in the computational speed of the spectral graph approach are expected through code optimization and code parallelization. This work has far-reaching practical implications for predicting thermal-induced defects in a variety of manufacturing processes including casting and additive manufacturing.

Keywords

Heat conduction; diffusion equation; discrete Laplacian matrix; Green's function; finite element analysis; additive manufacturing

¹corresponding author, kcole1@unl.edu, 1-402-472-5857

1 Introduction

Objective and Motivation 1.1

In this paper a spectral graph (SG) approach is developed for quantitative thermal modeling. The SG approach enables rapid thermal simulation in a physical object through a pragmatic balance of precision and computation speed. The precision of the SG approach is found by comparison with benchmark heat transfer problems, specifically, one and three-dimensional bodies with planar boundaries for which exact analytical solutions are available.

The heat conduction problem to be solved in this work is stated using vector notation, as follows:

$$\frac{\partial T}{\partial t} = \alpha \nabla^2 T \text{ (domain R)}$$
 (1)

$$\frac{\partial T}{\partial t} = \alpha \nabla^2 T \text{ (domain R)}$$

$$\frac{\partial T}{\partial n} = 0 \text{ (boundary of R)}$$

$$T(x, y, z, t = 0) = T_0(x, y, z) \text{ (initial condition)}$$
(2)

$$T(x, y, z, t = 0) = T_0(x, y, z)$$
 (initial condition) (3)

Here T is temperature (K), (x, y, z) is spatial location in the body, t is time (s), n is the outward-facing unit vector (m) which has direction normal to the boundary, α is thermal difussivity (m²/s), and T_0 is the initial temperature. The Laplacian operator ∇^2 describes the spatial-diffusion portion of the heat conduction equation for any orthogonal coordinate system, in one, two or three dimensions. The above form of the heat conduction equation implicitly assumes that the thermal property α is independent of temperature.

Note that the SG approach described here is limited to a body with insulated boundaries, i.e., the Neumann (type 2) boundary condition (Eq. (2)). In future work the method will be extended to include Dirichlet (type 1) and Robin (type 3) boundary conditions.

1.2 Background

In this section the literature of the SG method is discussed in the context of the heat conduction equation. Recently the SG method has been used to solve the heat conduction equation in the context of image processing and filtering of other large data sets [1, 2]. A review paper by Solomon [3] discusses discrete differential operators that arise from partial differential equations such as the heat conduction equation; it shows that the Laplacian matrix constructed from a uniformly spaced grid gives a solution to the heat conduction equation. However, if the grid is not equally spaced, the relationship to the correct solution of the heat conduction equation is not clear.

In a study of geometric surface smoothing, Belkin et al. [4] show that the discrete Laplacian matrix obtained from spectral graph theory approaches the continuous Laplacian (∇^2 in Eq. 1) in the limit as the grid becomes sufficiently fine, even if the grid pattern is nonuniform. In a study of image smoothing, Zhang and Hancock use randomly assigned node locations to construct a discrete Laplacian matrix and subsequently to solve the heat conduction equation [1].

The graph-theoretic approach is distinct from several mesh-free methods developed previously. The peridynamic method was developed for systems undergoing dynamic cracking [5, 6]. The peridynamic method is meshfree in the sense that only the bonds between node points are tracked as the body deforms (bonds change length) or cracks (bonds break). The governing equation for each node is developed from an integral balance on force (or energy) in a neighborhood around each node. The peridynamic method requires a standard matrix inversion at each time step, similar to finite-element methods.

The spectral collocation method uses splines to provide an *a priori* functional form of the solution as part of a standard matrix inversion process [7, 8]. The moving particle system method was developed for free-surface fluid-flow problems, and it has recently been applied to heat conduction [9, 10]. The heat conduction equation is discretized by use of a Laplacian matrix with weighting functions that involve the square of the distance between the nodes. The resulting matrix form of the heat conduction equation requires a standard matrix inversion at each of many small time steps, similar to finite element methods.

1.3 Overview of the Paper

The paper is divided into six sections. Section 2 is an introduction of the spectral graph method applied to heat conduction. Section 3 explores a one-dimensional example to show the details of SG method, and compares the resulting solution with an exact analytical solution and with the finite difference method. Section 4 provides a three-dimensional case of the SG method and a procedure to calibrate the model parameters based on solutions from the exact analytical solution. The three-dimension heat transfer problem is also solved using the finite element method implemented in a commercial solver (Abaqus). Section 5 demonstrates the practical utility of the SG approach in the context of the additive

manufacturing (3D printing) process. Specifically, the SG method is used to predict the temperature distribution for an additively manufactured part with overhangs and undercuts. The same part is also simulated with a commercial finite element solver and the predictions are compared with the those obtained from the SG method. Section 6 contains a summary and discussion of future work.

$\mathbf{2}$ Spectral Graph Method (SG)

In this section the SG method is introduced using vector notation independent of the spatial details of the problem. Later specific examples of the SG method will be presented for a one-dimension problem and for a three-dimension problem.

First, dimensionless variables are introduced in Eq. (1) - Eq. (3), as follows:

$$\tilde{T} = T/T_1; \quad \tilde{t} = \alpha t/\ell^2; \quad \tilde{n} = n/\ell$$
 (4)

where ℓ is a characteristic length and T_1 is a characteristic temperature. Subsequently, the dimensionless heat conduction problem has the following form:

$$\frac{\partial \tilde{T}}{\partial \tilde{t}} = \tilde{\nabla}^2 \tilde{T} \text{ (domain R)}$$
 (5)

$$\frac{\partial \tilde{T}}{\partial \tilde{n}} = 0 \text{ (boundary of R)}$$
 (6)

$$\tilde{T}(\tilde{x}, \tilde{y}, \tilde{z}, \tilde{t} = 0) = \tilde{T}_0(\tilde{x}, \tilde{y}, \tilde{z}) \text{ (initial condition)}$$
 (7)

where $\tilde{\nabla}^2$ is the dimensionless Laplacian differential operator.

The spectral graph theory approach replaces the spatial derivatives represented by the continuous Laplacian operator $(\tilde{\nabla}^2)$ in the heat conduction equation, Eq. (5), by a discrete matrix called the Laplacian matrix (L), as well as the continuously varying temperature (\tilde{T}) by a vector of discrete temperatures (\tilde{T}) at node points in the domain. The discrete form of the above heat conduction problem may be written as

$$\frac{\partial \tilde{T}}{\partial \tilde{t}} = -L\tilde{T} \text{ (domain R)}$$

$$\frac{\partial \tilde{T}}{\partial \tilde{n}} = 0 \text{ (boundary of R)}$$
(8)

$$\frac{\partial \tilde{T}}{\partial \tilde{n}} = 0 \text{ (boundary of R)} \tag{9}$$

$$\tilde{T}\Big|_{\tilde{t}=0} = \tilde{T}_0 \text{ (initial condition)}$$
 (10)

Note the sign change in Eqn. (8), as the Laplacian matrix L from graph theory is defined with sign opposite to that of the continuous Laplacian operator $(\tilde{\nabla}^2)$. Construction of the Laplacian matrix is discussed later in section 3.2 and will be shown to be symmetric and diagonally dominant. At present the solution to the discrete heat conduction equation will be provided in matrix form.

The next step is to solve the following well-known eigenvalue problem, using standard matrix methods. Laplacian matrix L satisfies the eigenvalue equation:

$$L\phi = \phi\Lambda \tag{11}$$

where ϕ is the orthogonal eigenvector matrix

 Λ is the diagonal eigenvalue matrix

The eigenvector matrix ϕ is orthogonal because \mathbf{L} is symmetric and diagonally dominant [3]. Since for an orthogonal matrix the transpose is equal to its inverse, the product of the eigenvector matrix and its transpose is the identity matrix. That is:

$$\phi \phi' = \phi \phi^{-1} = \mathbf{I} \tag{12}$$

Using this property, post-multiply the eigenvalue equation, Eq. (11), by the matrix ϕ' :

$$L\phi\phi' = \phi\Lambda\phi'$$

$$LI = \phi\Lambda\phi'$$

$$L = \phi\Lambda\phi'$$
(13)

Replace this result into the discrete diffusion equation, Eq. (8):

$$\frac{\partial \tilde{T}}{\partial \tilde{t}} = -(\phi \Lambda \phi') \tilde{T} \tag{14}$$

This above equation is a first order matrix differential equation whose solution, subject to insulated boundaries, has the form of a matrix exponential [1, 3]:

$$\tilde{\boldsymbol{T}} = e^{-\phi\Lambda\phi'\tilde{t}}\tilde{\boldsymbol{T}}_0 \tag{15}$$

Recall that T_0 is the initial temperature vector. Next the exponential in the above solution will be expanded using a Taylor series. The exponential of matrix u is given by

$$e^{-u} = I - \frac{u}{1!} + \frac{u^2}{2!} - \frac{u^3}{3!} + \dots$$

Apply the above Taylor series expansion to the exponential term from Eq. (15), and simplify:

$$e^{-\phi\Lambda\phi'\tilde{t}} = I - \tilde{t}\frac{\phi\Lambda\phi'}{1!} + \tilde{t}^{2}\frac{(\phi\Lambda\phi')^{2}}{2!} - \tilde{t}^{3}\frac{(\phi\Lambda\phi')^{3}}{3!} + \dots$$

$$= I - \tilde{t}\frac{\phi\Lambda\phi'}{1!} + \tilde{t}^{2}\frac{(\phi\Lambda\phi')(\phi\Lambda\phi')}{2!} - \tilde{t}^{3}\frac{(\phi\Lambda\phi')(\phi\Lambda\phi')(\phi\Lambda\phi')}{3!} + \dots$$

$$= I - \frac{\phi(\Lambda\tilde{t})\phi'}{1!} + \frac{(\phi(\Lambda\tilde{t})^{2}\phi')}{2!} - \frac{(\phi(\Lambda\tilde{t})^{3}\phi')}{3!} + \dots$$

$$= \phi \left[I - \frac{\Lambda\tilde{t}}{1!} + \frac{(\Lambda\tilde{t})^{2}}{2!} - \frac{(\Lambda\tilde{t})^{3}}{3!} + \dots\right]\phi'$$

$$= \phi \left[e^{-\Lambda\tilde{t}}\right]\phi'$$
(16)

The final exponential argument contains only the eigenvalue matrix multiplied by time. With this simplification the temperature solution is given by

$$\tilde{T} = \phi e^{-\Lambda \tilde{t}} \phi' \, \tilde{T}_0 \tag{17}$$

In this solution, the spatial behavior is embodied in the eigenfunction matrix ϕ and the timeevolution behavior is embodied in the eigenvalue matrix Λ . At small values of time, many eigenvalues within the matrix exponential $e^{-\Lambda \tilde{t}}$ contribute to the temperature distribution. At large values of time, however, the temperature depends only on the smallest non-zero eigenvalue (also called the Fiedler eigenvalue Λ_2), which determines the rate at which the temperature decays toward the final (steady) value. This is analogous to the effect of time on the number of series terms needed from a Fourier-series solution of the continuum heat conduction equation.

3 One-Dimensional Example

In this section a one-dimensional (1D) heat conduction problem is solved using the exact analytical method and the resulting solution is compared with the SG and finite difference (FD) methods.

3.1 1D Exact Analytical Solution

Consider the following 1D problem with a piecewise initial condition and insulated (Neumann) boundaries:

$$\frac{1}{\alpha} \frac{\partial T}{\partial t} = \frac{\partial^2 T}{\partial x^2} \tag{18}$$

at
$$x = 0$$
, $\frac{\partial T}{\partial x} = 0$ (19)

at
$$x = \ell$$
, $\frac{\partial x}{\partial T} = 0$ (20)

at
$$t = 0$$
, $T(x,0) = \begin{cases} T_1; & 0 < x < a \\ 0; & \text{otherwise} \end{cases}$ (21)

This problem is denoted case X22B00T5 in the numbering system for heat conduction [11, chap. 2]. An exact analytic solution for this problem is given by [12, p. 101]

$$T(x,t) = T_1 \left[\frac{a}{\ell} + 2 \sum_{m=1}^{\infty} \frac{e^{-m^2 \pi^2 \alpha t/\ell^2}}{m\pi} \cos \frac{m\pi x}{\ell} \sin \frac{m\pi a}{\ell} \right]$$
 (22)

3.2 1D Spectral Graph Method

In this section the Laplacian matrix will be constructed with the operational steps provided by spectral graph theory [3]. The first step is to find the distance between nodes i and j which are located at coordinates x_i and x_j .

For the one-dimensional problem, the distance is,

$$c_{ij} = \sqrt{(x_i - x_j)^2}$$

Weights are assigned to each edge (connection between nodes) which depend on the distance between the nodes. The edge weights can take various forms, but to agree with the finitedifference formulation, the edge weights are given by

$$a_{ij} = \begin{cases} \frac{1}{c_{ij}^2}; & c_{ij} \le b \text{ and } i \ne j \\ 0; & c_{ij} > b \text{ or } i = j \end{cases}$$
 (23)

where b is called the neighborhood distance. All the nodes inside the neighborhood distance are connected to each other. For i = j the edge weight is zero so that a node is not connected to itself (avoiding cycles within a graph). Also to agree with 1D finite difference,

the neighborhood distance is the node spacing b = dx. In other words, the nodes are equi-spaced.

The adjacency matrix is a matrix containing these weights:

$$\mathbf{A} = \begin{bmatrix} 0 & \frac{1}{b^2} & 0 & \cdots & 0 \\ \frac{1}{b^2} & 0 & \frac{1}{b^2} & & \\ 0 & \ddots & \ddots & \ddots & \vdots \\ \vdots & & \frac{1}{b^2} & 0 & \frac{1}{b^2} \\ 0 & \cdots & 0 & \frac{1}{b^2} & 0 \end{bmatrix}$$
 (24)

Next the sum across rows of the adjacency matrix is constructed:

$$d_i = \sum_i a_{ij}$$

and assembled into the degree matrix which is a diagonal matrix:

$$\mathbf{D} = \frac{1}{b^2} \begin{bmatrix} 1 & 0 & 0 & \cdots & 0 \\ 0 & 2 & 0 & & \\ 0 & & \ddots & & \vdots \\ \vdots & & 0 & 2 & 0 \\ 0 & \cdots & 0 & 0 & 1 \end{bmatrix}$$
 (25)

Finally, the Laplacian matrix is constructed by subtracting the adjacancy matrix from the degree matrix as L = D - A, as follows:

$$L = \frac{1}{b^2} \begin{bmatrix} 1 & -1 & 0 & \cdots & 0 \\ -1 & 2 & -1 & \cdots & 0 \\ 0 & \ddots & \ddots & \ddots & \vdots \\ \vdots & -1 & 2 & -1 \\ 0 & \cdots & 0 & -1 & 1 \end{bmatrix}$$
 (26)

The Laplacian constructed in this way for the one-dimensional problem with uniform node spaceing is the same as the finite difference matrix discussed in the next sub-section. It is important to note that this development gives the Laplacian for insulated (Neumann, type 2) boundaries.

3.3 1D Finite Difference Method

The Laplacian matrix will be constructed using the finite volume method - an energy balance approach traditionally used to develop the finite difference method from first principles. This study will also demarcate the conditions under which the spectral graph solution of the heat conduction problem converges to the finite difference formulation in one dimension.

Consider the one-dimensional heat conduction equation for the Cartesian wall with the domain (0 < x < L) discretized with uniformly-spaced node points. For an interior node, the energy balance based on the first law of thermodynamics has the form

(heat storage in the volume) = (heat flow into the volume)
$$CV \frac{\partial T}{\partial t} = Q_e + Q_w$$
 (27)

Here C (J/K/m³) is volumetric heat capacity, V (m³) is node volume, Q_e and Q_w (Watts) are heat flows across the node boundaries. While in this development there are no internal sources of heat, nevertheless, these could be added to the right-hand side. Refer to Fig. 1. For the finite difference method the heat flows are given by [13, p. 46]

$$Q_w = kA \frac{T_w - T}{dx}; \quad Q_e = kA \frac{T_e - T}{dx}$$
(28)

where k (W/m/K) is thermal conductivity, A (m²) is the area for heat flow at the node

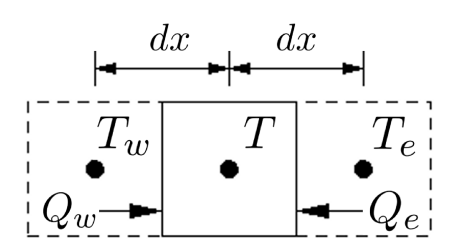


Figure 1: Geometry for heat flow to interior node on a uniformly-spaced grid.

boundary, dx (m) is the node spacing, and T_e and T_w (K) are the temperatures at the east and west neighboring nodes, respectively. Next dimensionless parameters will be introduced as follows:

$$\tilde{T} = \frac{T}{T_1}; \quad \tilde{t} = \frac{\alpha t}{\ell^2}; \quad \tilde{d}x = \frac{dx}{\ell}; \quad \tilde{Q} = \frac{Q}{kT_1\ell}; \quad \tilde{A} = \frac{A}{\ell^2}; \quad \tilde{V} = \frac{V}{\ell^3}; \quad \alpha = \frac{k}{C}$$
(29)

Where T_1 is a characteristic temperature, ℓ is a characteristic length, and α is thermal diffusivity (m²/s). Introducing these parameters into the energy equation, and including

the heat fluxes, the energy equation may be shown to have the form:

$$\tilde{V}\frac{\partial \tilde{T}}{\partial \tilde{t}} = \tilde{Q}_e + \tilde{Q}_w \tag{30}$$

The normalized heat fluxes are given by:

$$\tilde{Q}_w = \frac{\tilde{A}}{\tilde{d}x}(\tilde{T}_w - \tilde{T}); \qquad \tilde{Q}_e = \frac{\tilde{A}}{\tilde{d}x}(\tilde{T}_e - \tilde{T})$$
 (31)

Combine the heat fluxes with the energy equation, divide by \tilde{V} , and recognize that for one-dimensional transfer $\tilde{V} = \tilde{A}\tilde{dx}$, the result is:

$$\frac{\partial \tilde{T}}{\partial \tilde{t}} = \frac{\tilde{A}}{\tilde{d}\tilde{x}\tilde{V}}(\tilde{T}_w - \tilde{T}) + \frac{\tilde{A}}{\tilde{d}\tilde{x}\tilde{V}}(\tilde{T}_e - \tilde{T})$$

$$= \frac{1}{\tilde{d}\tilde{x}^2} \left(\tilde{T}_w - 2\tilde{T} + \tilde{T}_e\right) \tag{32}$$

The above energy equation applies to all interior nodes. At the left boundary let $Q_w = 0$ and at the right boundary let $Q_e=0$ to describe insulated boundaries (homogenesous Neumann condition). Then the boundary node equations have the form

left boundary:
$$\frac{\partial \tilde{T}}{\partial \tilde{t}} = \frac{1}{\tilde{dx}^2} \left(\tilde{T}_e - \tilde{T} \right)$$
(33)
right boundary:
$$\frac{\partial \tilde{T}}{\partial \tilde{t}} = \frac{1}{\tilde{dx}^2} \left(\tilde{T}_w - \tilde{T} \right)$$
(34)

right boundary:
$$\frac{\partial \tilde{T}}{\partial \tilde{t}} = \frac{1}{\tilde{dx}^2} \left(\tilde{T}_w - \tilde{T} \right)$$
 (34)

If the interior node equation, Eq. (23), is repeated for every interior node and combined with the boundary-node equations above, a matrix form comprising all node equations has the form

$$\frac{\partial}{\partial \tilde{t}} \begin{bmatrix} \tilde{T}_1 \\ \tilde{T}_2 \\ \vdots \\ \tilde{T}_n \end{bmatrix} = -\frac{1}{\tilde{dx}^2} \begin{bmatrix} 1 & -1 & 0 & \cdots & 0 \\ -1 & 2 & -1 & & \\ 0 & & \ddots & & \vdots \\ \vdots & & -1 & 2 & -1 \\ 0 & \cdots & 0 & -1 & 1 \end{bmatrix} \begin{bmatrix} \tilde{T}_1 \\ \tilde{T}_2 \\ \vdots \\ \tilde{T}_n \end{bmatrix}$$
(35)

Note that a minus sign before the right-hand side is included so that the square matrix is identical to the Laplacian matrix (L) developed in the previous section for the SG method. Pertinently, the Laplacian in Eq. 35 developed from the FD method is also real, diagonally dominant, and symmetric, and was developed for homogeneous type 2 (Neumann) boundary conditions. Homogeneous boundary conditions of type 1 and 3 are also possible but are not treated in this paper.

To complete the finite difference approach, the time derivative $(\frac{\partial}{\partial t})$ must also be approximated by a time-wise difference, and then a matrix solution must be carried out to solve for the temperature at each time step (see for example [13, p. 54]). However, these well-known details are omitted for the purpose of brevity.

3.4 1D Results: Compare FD and SG Solutions

Results for the one-dimensional example problem are given in this section. The SG method was implemented in Matlab. Standard matrix methods were used to find the eigenvalues and eigenvectors of the Laplacian matrix, and to carry out matrix multiplication for the SG temperature solution in Eq. (17). The one-dimensional SG results were verified by comparison with the exact solution and with a fully-implicit FD solution using the same uniformly spaced grid points.

A three-way comparison between the SG solution (Eq. 17), a fully-implicit FD solution (Eq. 35), and the exact solution (Eq. 22) is shown in Fig. 2, which contains two plots of temperature versus time at the centerline of the body ($\tilde{x}=0.5$). For nx= 21 spatial nodes, both the SG and FD methods overshoot the correct temperature by about 10 % at $\tilde{t}=0.1$. For nx = 101 the error at $\tilde{t}=0.1$ is below one percent. The maximum time t=0.2 was chosen because the temperature at x/L=0.5 has essentially reached its final value for initial heating condition a/L=0.238. A more complete picture of the error relative to the exact solution is found by examining the symmetric mean absolute percent error (SMAPE) over the time range. Let T_{ex} be the exact temperature and let T_{sg} be the spectral graph temperature, evaluated at the center of the body. Then the SMAPE error is given by

SMAPE =
$$\frac{1}{m} \sum_{i=1}^{m} \frac{|T_{ex}(t_i) - T_{sg}(t_i)|}{T_{ex}(t_i) + T_{sg}(t_i)} \times 100\%$$
 (36)

where m is the number of timesteps. Values for the SMAPE error for both the SG and the FD solutions are given in Table 1. The error is sensitive to spatial discretization, decreasing with inverse proportion to the number of spatial nodes as nx changes from 11 to 1001. An odd number of nodes was used to place a node precisely at x/L = 0.5 to facilitate comparison among different cases. The time step size has no influence at all on the error for the SG method, because in the SG solution the temperature is computed from the initial

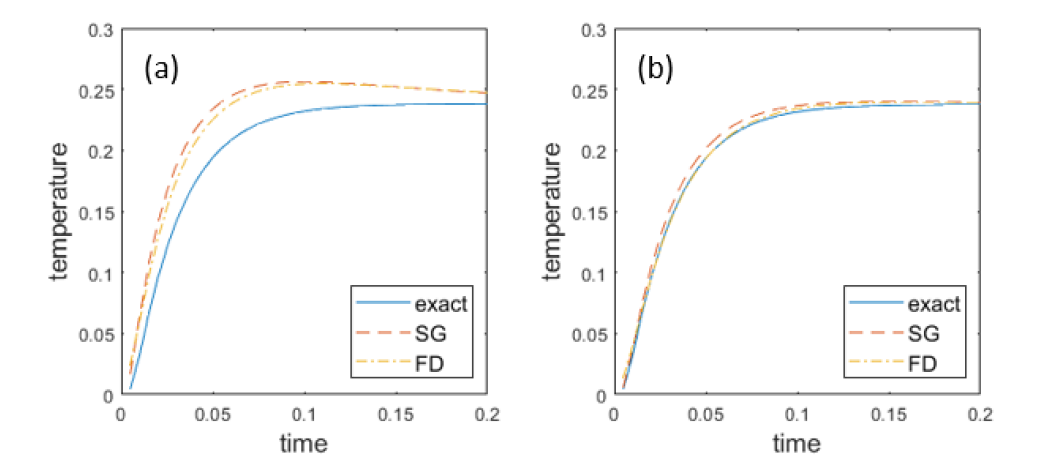


Figure 2: Compare SG method, FD method, and exact solution at x/L = 0.5 for (a) 21 spatial nodes (b) 101 spatial nodes. The initially heated region is of size (0 < x/L < 0.238).

temperature multiplied by a time-exponential. No intervening time steps are involved. For this one-dimensional problem, nx = 11 nodes are sufficient to provide results within 10 % SMAPE error. In a similar vein, the FD error decreases slightly as more time steps are added (smaller timestep size, nt) when nx = 11 and nx = 21. On the other hand the FD error increases slightly as timesteps are added for spatial discretization nx = 101 and nx = 1001. The table shows that when the timestep size changes by a factor of 10, the FD error changes but little, which suggests that the FD error is insensitive to timestep size. Important behaviors observed in the FD error, shown in Table 1, are as follows. First, the FD error values are of the same order as the SG errors. Second, for very small timesteps (nt = 4000) the FD error values approach the SG error values. To repeat, the solutions from the FD and SG method converge, errorwise, when the timestep size is sufficiently small.

4 Three-Dimensional Example

In the preceding sections, a one-dimensional heat conduction problem was used to demonstrate the SG method and to quantity the precision of the solution. In this section the solution from the exact analytical, SG, and FE methods are compared in the context of a three-dimension object. First, the exact analytical solution for a three-dimension (3D) body is given. Next, the SG solution to the three-dimensional case is provided, followed by

Table 1: Symmetric mean absolute percentage error (SMAPE) in SG and FD values, compared to the exact temperature, versus number of spatial nodes nx and time steps nt. The comparison is made at the center of the body over the time range (0,0.2) and the body is initially heated over $(0 < \tilde{x} < 0.238)$.

		SG	FD
nx	nt	SMAPE	SMAPE
11	40	6.783405	7.056041
21	40	3.713437	3.841302
101	40	0.783407	0.772047
1001	40	0.079316	0.033775
11	400	6.783405	6.811669
21	400	3.713437	3.727278
101	400	0.783407	0.783257
1001	400	0.079316	0.075729
11	4000	6.783405	6.786241
21	4000	3.713437	3.714831
101	4000	0.783407	0.783401
1001	4000	0.079316	0.078966

implementation of an FE model for the same case. This section also provides a guideline for calibrating the SG method through the exact analytical method.

4.1 3D Exact Analytical Solution

Consider heat conduction in a parallelepiped a piecewise initial condition and with insulated boundaries. The geometry is shown in Fig. 3. The temperature in the parallelepiped

satisfies the following energy equation and boundary conditions:

$$\frac{\partial^2 T}{\partial x^2} + \frac{\partial^2 T}{\partial y^2} + \frac{\partial^2 T}{\partial z^2} = \frac{1}{\alpha} \frac{\partial T}{\partial t}; \begin{cases}
0 < x < L \\
0 < y < W \\
0 < z < H \\
t > 0
\end{cases}$$
at boundary i ,
$$k \frac{\partial T}{\partial n_i} = 0, \quad i = 1, 2, 3, 4, 5, 6$$
(38)

at boundary
$$i$$
, $k \frac{\partial T}{\partial n_i} = 0$, $i = 1, 2, 3, 4, 5, 6$ (38)

$$T(x, y, z, 0) = \begin{cases} T_0; & 0 < x < L_1, & 0 < y < W_1, & 0 < z < H_1 \\ 0; & \text{otherwise} \end{cases}$$
(39)

The temperature at large values of the time is given by [14]:

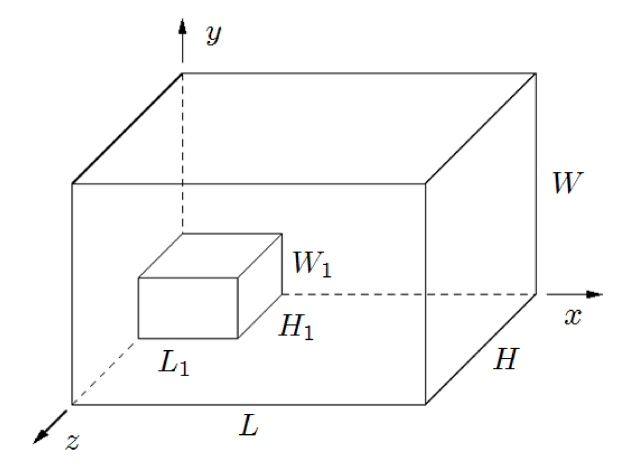


Figure 3: Geometry for exact temperature solution applied to calibration: parallelepiped with piecewise initial condition and insulated boundaries.

$$\tilde{T}(\tilde{x}, \tilde{y}, \tilde{z}, \tilde{t}) = \left[\tilde{L}_1 + 2 \sum_{m=1}^{\infty} \exp(-m^2 \pi^2 \tilde{t}) \frac{\cos(m\pi \tilde{x}) \sin(m\pi \tilde{a})}{m\pi} \right] \\
\times \left[\tilde{W}_1 + 2 \sum_{n=1}^{\infty} \exp(-n^2 \pi^2 \tilde{t}/\tilde{W}^2) \frac{\cos(n\pi \tilde{y}) \sin(n\pi \tilde{W}_1)}{n\pi} \right] \\
\times \left[\tilde{H}_1 + 2 \sum_{p=1}^{\infty} \exp(-p^2 \pi^2 \tilde{t}/\tilde{H}^2) \frac{\cos(p\pi \tilde{z}) \sin(p\pi \tilde{H}_1)}{p\pi} \right]$$
(40)

The above temperature expression contains three infinite series that converge slowly at small time, which is why the following small-time form is important. For small time, defined by $\tilde{t} < 0.01$, use:

$$\tilde{T}(\tilde{x}, \tilde{y}, \tilde{z}, \tilde{t}) = \frac{1}{4} \left[\operatorname{erf} \left(\frac{\tilde{x} + \tilde{L}_{1}}{\sqrt{4\tilde{t}}} \right) - \operatorname{erf} \left(\frac{\tilde{x} - \tilde{L}_{1}}{\sqrt{4\tilde{t}}} \right) - \operatorname{erf} \left(\frac{2 - \tilde{x} - \tilde{L}_{1}}{\sqrt{4\tilde{t}}} \right) + \operatorname{erf} \left(\frac{2 - \tilde{x}}{\sqrt{4\tilde{t}}} \right) \right] \\
\times \left[\operatorname{erf} \left(\frac{\tilde{W}(\tilde{y} + \tilde{W}_{1})}{\sqrt{4\tilde{t}}} \right) - \operatorname{erf} \left(\frac{\tilde{W}(\tilde{y} - \tilde{W}_{1})}{\sqrt{4\tilde{t}}} \right) \right] \\
- \operatorname{erf} \left(\frac{\tilde{W}(2 - \tilde{y} - \tilde{W}_{1})}{\sqrt{4\tilde{t}}} \right) + \operatorname{erf} \left(\frac{\tilde{W}(2 - \tilde{y})}{\sqrt{4\tilde{t}}} \right) \right] \\
\times \left[\operatorname{erf} \left(\frac{\tilde{H}(\tilde{z} + \tilde{H}_{1})}{\sqrt{4\tilde{t}}} \right) - \operatorname{erf} \left(\frac{\tilde{H}(\tilde{z} - \tilde{H}_{1})}{\sqrt{4\tilde{t}}} \right) \right] \\
- \operatorname{erf} \left(\frac{\tilde{H}(2 - \tilde{z} - \tilde{H}_{1})}{\sqrt{4\tilde{t}}} \right) + \operatorname{erf} \left(\frac{\tilde{H}(2 - \tilde{z})}{\sqrt{4\tilde{t}}} \right) \right] \tag{41}$$

The dimensionless variables used in the above expression are defined by

$$\tilde{x} = \frac{x}{L}; \quad \tilde{y} = \frac{y}{W}; \quad \tilde{z} = \frac{z}{H}; \quad \tilde{W} = \frac{W}{L}; \quad \tilde{H} = \frac{H}{L};$$

$$\tilde{L}_1 = \frac{L_1}{L}; \quad \tilde{W}_1 = \frac{W_1}{W}; \quad \tilde{H}_1 = \frac{H_1}{H}; \quad \tilde{t} = \frac{\alpha t}{L^2}; \quad \tilde{T} = \frac{T}{T_0}$$
(42)

Figure 4 shows values from the above exact solution for the temperature history at four points in an equal-sided parallelepiped (cube) initially heated over one-eight of its volume $(L_1 = W_1 = H_1 = 0.5)$, so that the final temperature is $T/T_0 = 0.5^3 = 0.125$. A full discussion of this solution, along with other plots and computer codes, is available elsewhere [14].

4.2 3D Spectral Graph Method

Construction of the Laplacian matrix for three-dimensional SG method is similar to the one-dimensional process discussed earlier, with two differences. The first difference is that the distance between nodes is found using the Euclidean norm in three-space, that is,

$$c_{ij} = \sqrt{(x_i - x_j)^2 + (y_i - y_j)^2 + (z_i - z_j)^2}$$

where (x_i, y_i, z_i) is the Cartesian coordinate of node i. The second difference is that the edge weights are chosen to have a Gaussian form:

$$a_{ij} = \begin{cases} e^{-c_{ij}^2/\sigma^2}; & c_{ij} \le b \text{ and } i \ne j \\ 0; & c_{ij} > b \text{ or } i = j \end{cases}$$

$$(43)$$

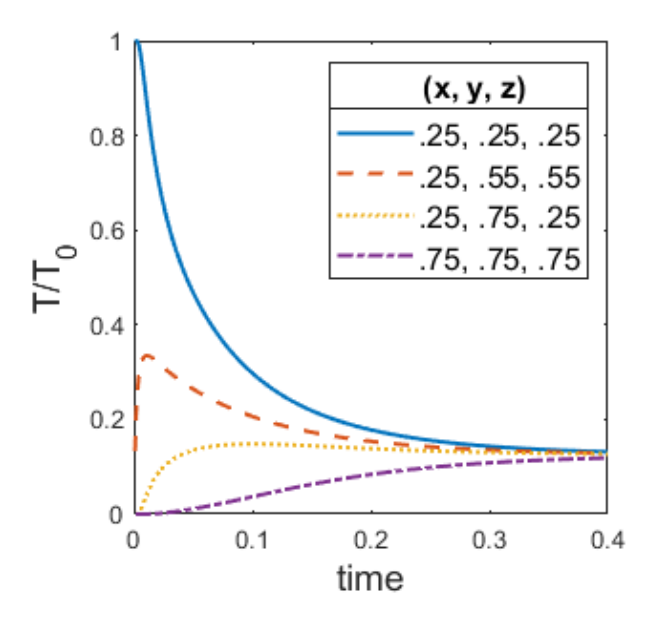


Figure 4: Temperature in a cube at four locations, one in the heated region and three in the unheated region. The initial temperature is $T/T_0 = 1$ in the region defined by $(L_1 = W_1 = H_1 = 0.5)$.

As before, b is the radius defining the neighborhood, within which each node is connected to its neighbors, and σ is the standard deviation of internodel distances c_{ij} . The Gaussian edge weights used here are taken from the graph theory literature (for example, [1]) and as such have no inherent connection to the heat conduction problem. Gaussian-distributed edge weights do have the benefit of an upper bound of unity when the internodal distance is very small, as can occur in a randomly distributed grid. In this way the heat flow at a single node is never singular (or nearly singular) as would occur for $c_{ij} \approx 0$ if the edge weight was $1/c_{ij}^2$ in the one-dimensional formulation discussed earlier.

The application of the SG method to three dimensional geometries involves random node placement and Gaussian edge weights. As noted above, because the Gaussian edge weights are not inherently connected to heat conduction, the results of the SG method must be appropriately scaled for heat conduction. A gain factor is used for this purpose which modifies the SG method solution given by Eq. (17) with factor g premultiplying time in the argument of the exponential term:

$$\tilde{T} = \phi e^{-g\Lambda \tilde{t}} \phi' \, \tilde{T}_0 \tag{44}$$

The effect of the gain factor (g) is to speed up or slow down the time rate of the thermal response. The correct choice of the gain factor, to calibrate the SG method for heat conduction, is carried out by comparing the SG solution to a known solution.

4.2.1 Procedure for node generation.

Several mesh-block geometries were created for the parallelepiped-shaped part by specifying the same number of blocks along each coordinate direction, n_b , and the number of grid points within each block, n_g . Table 2 shows the total number of nodes in a mesh created from different combinations of n_b and n_g . For example, $n_b = 4$ and $n_g = 3$ give the total number of points as $4 \cdot 4 \cdot 4 \cdot 3 = 192$. To study the effect of random node locations within blocks, ten meshes were created by different random embodiments of each blockgrid combination studied, and many of the results are reported as the mean and variance over these ten meshes. To avoid the possibility of too-close mesh points, the randomly determined points in each block were sampled from a finely divided grid placed on each block, without replacement. Usually the block was subdivided into 1000 locations.

Table 2: Number of mesh points in a parallelepiped body created by n_b blocks along each axis and n_g grid points within each block. Total number of mesh points = $n_b^3 \cdot n_g$.

	n_g				
n_b	3	4	5	6	
4	192	256	320	384	
6	648	864	1080	1296	
8	1536	2048	2560	3072	

4.2.2 Sensitivity of the gain factor.

A sensitivity study was carried out to explore the impact of time range and temperatureobservation location on the optimal gain factor. The purpose is to find the gain factor (g). To investigate the sensitivity, the normalized sensitivity coefficient was found in the form

$$X = g \frac{\partial T_j(t)}{\partial q} \tag{45}$$

where T is evaluated from the SG method and subscript j represents a particular location in the body. Three locations in the body were studied using a finite-difference approximation to the above derivative. Figure 5 shows the sensitivity coefficient at three locations along the corner-corner diagonal in the cube as shown: in the center of the heated region at x/L = y/L = z/L = 0.25; at the center of the cube; and, in the unheated region at x/L = y/L = z/L = 0.75. The sensitivity to the gain at these locations is plotted versus time to show that the heated region provides the largest sensitivity with a peak at $\tilde{t} = 0.05$. The sensitivity in the unheated region has a smaller peak at $\tilde{t} = 0.16$. The error bars are the standard deviation over ten grids, meshed with 216 blocks (arranged 6x6x6) each of which contains 5 randomly-placed nodes for n = 1080 nodes. Sensitivity results are similar for other node combinations (not shown).

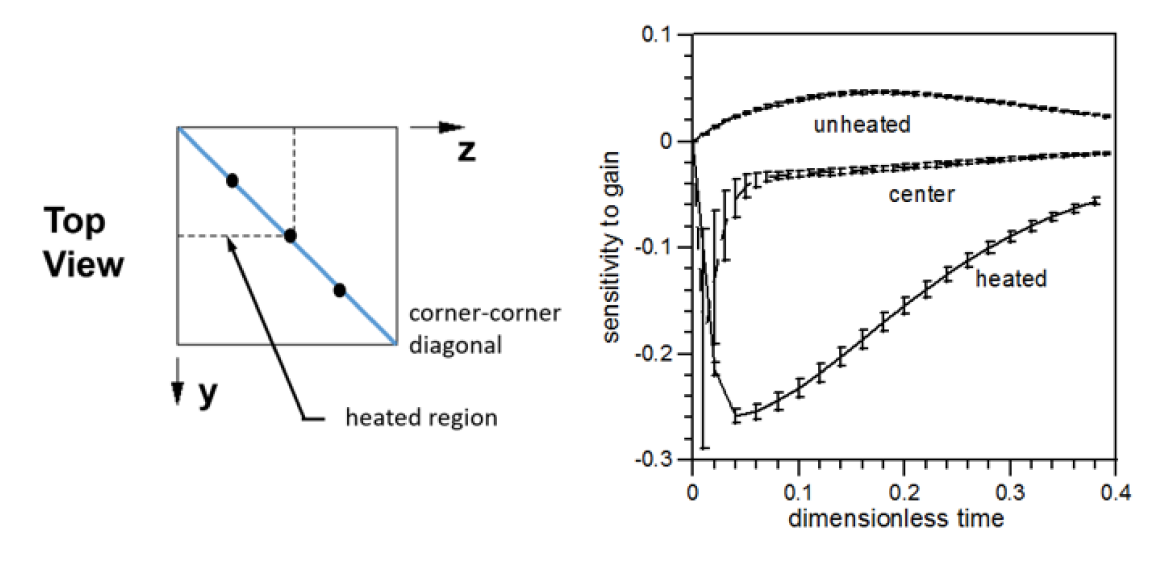


Figure 5: Sensitivity to gain at three locations along the corner-corner diagonal in the cube as shown. The error bars are the standard deviation over ten grids, meshed with 216 blocks (arranged 6x6x6) each of which contains 5 randomly-placed nodes for n = 1080 nodes.

4.3 Calibration Procedure

The SG method for solving the heat conduction equation was developed for *qualitative* applications such as image smoothing. For applications where *quantitiative* results are needed, calibration of the SG method is required.

Like all numerical methods, the SG method introduces numerical parameters that have to be reconciled with the physical domain of interest. In the SG method, such numerical parameters include the number of spatial nodes, the distribution of these nodes, and the manner in which nodes are connected. These numerical parameters must be chosen so that the solution is insensitive to these introduced parameters while providing acceptable precision, usually determined by comparison with benchmark problems.

An exact solution in a regular-shaped body (parallelepiped) was used as the standard against which the SG solution was compared, and a sensitivity study was used to determine the best spatial location(s) and the best time domain over which the SG method should be calibrated.

The calibration procedure for obtaining the gain factor involves a rigorous comparison between the SG method and the exact solution discussed earlier in Section 4.1. Such comparisons are variously termed regression analysis, parameter estimation, or data fitting [15, p. 2]. The benchmark data for the comparison is the time history of the temperature from the exact solution in the time range (0,0.4) at the center of the initially heated region for a cubic body. Twenty temperature values at uniformly-spaced time points were used. The initially heated region is of size $L_1 = W_1 = H_1 = 0.5$ as defined in Eq. (42).

The baseline for the comparison is the SG method evaluated at the same space and time locations in a similarly heated cube. Because the SG method produces temperatures only at node locations which are randomly distributed within blocks, an interpolation procedure was used to find the temperature at the precise locations desired; the Matlab routine 'griddata' was used for this purpose. In contrast, no interpolation is needed for the time coordinate.

The data fitting procedure was the minimization of the sum-of-square error between the exact solution and the SG model. The data fitting was carried out with a Gauss-Newton method [15, p. 29] which converged to four-digit precision in about six iterations; the resulting gain factor was not sensitive to the initial guess.

Although in this study a simple body shape is used, for a more complex shape such as that simulated in Sec. 5 in the context of additive manufacturing, the calibration could be carried out by comparison with a commercial FE solver.

4.3.1 Calibration results.

The gain factor was explored for the impact of two numerical parameters introduced by the SG method, specifically, the total number of nodes n_{tot} and the neighborhood radius b. Figure 6a shows that the gain is inversely proportional to the total number of nodes because constant gain (g) multiplied by n_{tot} is constant. In this plot each data point is the mean gain and the error bars are the variance from studying ten randomly constructed meshes for each n_{tot} . Figure 6b shows the gain values plotted versus neighbor radius b. The gain decreases as the neighborhood radius increases, roughly proportional to the neighbor radius to the power minus two (the best-fit curve shown in Fig 6a is proportional to $b^{-2.1}$, very close to b^{-2}). A scaling argument to explain this inverse-square law is tendered in the next section.

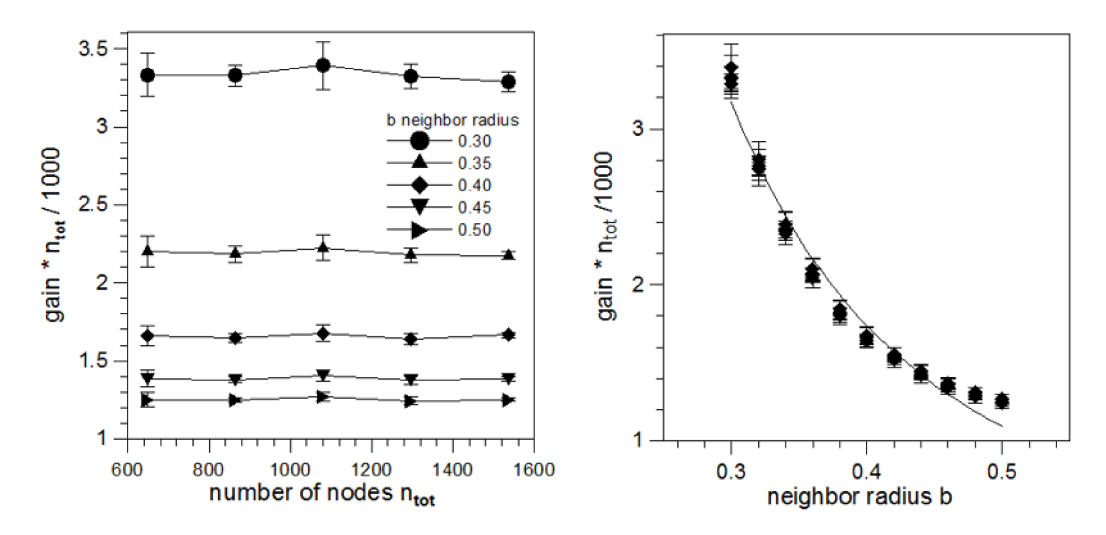


Figure 6: Gain multiplied by n_{tot} from the SG method is (a) plotted versus total number of nodes to show that gain is inversely proportional to n_{tot} ; and (b) is plotted versus the neighbor radius to show a power-law dependence.

4.3.2 Scaling of the gain factor.

A scaling argument is provided to explain the observed variation of the gain factor with the number of nodes and with the neighborhood size. The argument is based on the physics of heat transfer to a single node from its neighbor nodes. Figure 7 shows a schematic of a node of interest at temperature T surrounded by several neighbor nodes within neighbor

radius b. The finite-volume heat conduction equation, given earlier in Eq. (23) for the one-dimensional heat transfer on a uniform grid, is extended to the SG method in three dimensions, as follows:

$$\frac{\partial \tilde{T}}{\partial \tilde{t}} = \sum_{i=1}^{n_b} \frac{\tilde{A}_i}{\tilde{d}_i \tilde{V}} (\tilde{T}_i - \tilde{T})$$
(46)

Here T is the temperature of the node of interest with storage volume V; T_i is the temperature at each of the n_b neighbor nodes; A_i is the area over which heat is transferred from node i; and, d_i is the distance to node i. Refer to Fig. 7. In the above equation, quantities $\tilde{A}_i/(\tilde{d}_i\tilde{V})$ are the edge weights in the Laplacian matrix – compare the above equation to Eq. (8) showing the discrete heat conduction equation with the Laplacian matrix. Consider a

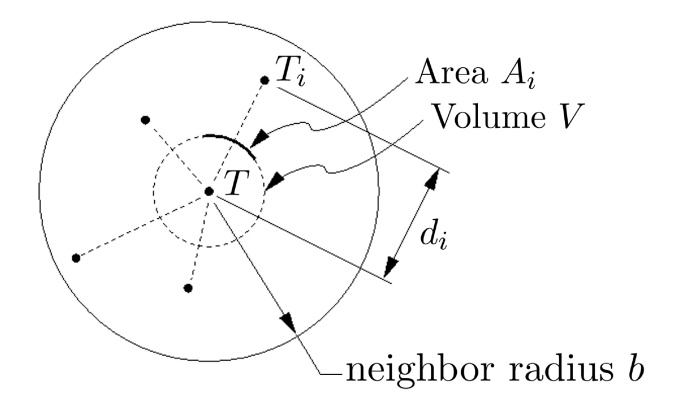


Figure 7: Neighborhood of radius b around node of temperature T and local volume V. Heat flow from neighbor node at temperature T_i takes place through area A_i across distance d_i .

mesh in which n_{tot} nodes are located at random locations throughout a body according to a uniform probability distribution. The neighborhood around one node is defined by neighbor radius \tilde{b} and there are n_b neighbor nodes closer than distance \tilde{b} . Next the general size of local volume \tilde{V} and heat-transfer area \tilde{A}_i will be determined. The shape of local volume \tilde{V} is not known, but its size can be characterized by a sphere of some unknown radius \tilde{r} that will be characterized later. That is, let

$$\tilde{V} = \frac{4}{3}\pi\tilde{r}^3 \tag{47}$$

Area \tilde{A}_i is that fraction of the surface of volume \tilde{V} associated with heat transfer from one neighbor node. As n_b is the number of neighbor nodes, on average area \tilde{A}_i may be

approximated by the appropriate fraction of the surface of local volume \tilde{V} , given by

$$\tilde{A}_i = \frac{4\pi\tilde{r}^2}{n_b} \tag{48}$$

Distance \tilde{d}_i to neighbor node i is something less than radius \tilde{b} ; let $\tilde{d}_i = s_1 \cdot \tilde{b}$ where s_1 is an unknown scale factor. The number of neighbor nodes must be proportional to the total number of nodes in the body n_{tot} , so let $n_b = s_2 \cdot n_{tot}$ where s_2 is another scale factor. Finally, let the radius of the local volume be some fraction of the neighbor radius, $\tilde{r} = s_3 \cdot \tilde{b}$ where s_3 is a third scale factor. Assemble these scaling relations into the weight factor from Eq. (46), the result is:

$$\frac{\tilde{A}_i}{\tilde{d}_i \tilde{V}} = \frac{4\pi (s_3 \tilde{b})^2 / (s_2 n_{tot})}{(s_1 \tilde{b}) \frac{4}{3} \pi (s_3 \tilde{b})^3} = \frac{3}{s_1 s_2 s_3} \frac{1}{\tilde{b}^2 n_{tot}}$$
(49)

The above result for the scaling argument is that the edge weight needed for the SG method is proportional to $1/(\tilde{b}^2 n_{tot})$, that is, inversely proportional to the square of the neighborhood radius and inversely proportional to the number of nodes in the body. This scaling relation explains the behavior of the gain factor when n_{tot} and b are varied in the calibration experiments described in the previous section.

4.3.3 Calibration Applied to Related Cases.

In this section the calibration gain factor, found once, is applied to related cases whose heating geometry or physical geometry is different from the calibration case. The purpose here is to ascertain the domain of applicability of one calibration to other cases. The calibration geometry is the unit cube initially heated over the smaller cube $L_1 = W_1 = H_1 = 0.5$, or one-eighth of the total volume.

Consider the SG applied to the unit cube where the amount of heat initially present is also one-eighth of the total volume, but the distribution of that heat varies. Some of the initial-heating geometries considered are shown in Fig. 8, where the central cube (red) is the cubic heated region used for calibration, and the (green) non-cubic shapes are heating shapes for the test cases. For each test geometry, the SG method was carried out using the calibration gain factor (gain values shown in Fig. 6) and the temperature was compared to the exact solution using the correct, non-cubic, initial heating condition. The error was computed for each geometry at six points on each of three diagonals: corner-to-corner; edge-to-edge; and, face-to-face. For each geometry the calculation was repeated:

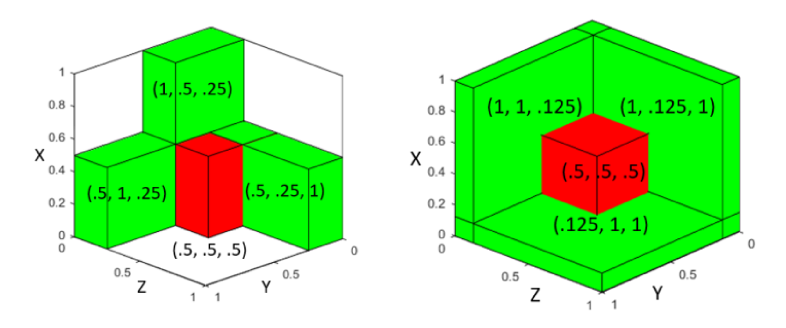


Figure 8: Cubic heating geometry (red) for calibration applied to several noncubic heating geometries (green) with equal initially-heated volume.

by varying the number of grid points $n_{tot} = 648$, 864, 1080, 1296, 1536; by varying the size of the neighborhood radius $\tilde{b} = 0.3$, 0.35, 0.4, 0.45, 0.5; and, by using 10 different (random) grids for each situation. It is important to note that the appropriate gain factor was used for each distinct value of neighborhood radius \tilde{b} . The mean error was computed by combining $3 \cdot 6 \cdot 5 \cdot 5 \cdot 10 = 4500$ comparisons with exact values, listed in Table 3. Each row in Table 3 gives the size of the initially-heated region, the final temperature, and the SMAPE and RMSE error defined earlier. The final normalized temperature is 1/8 for all these cases because the body is initially heated over 1/8 of the volume, and energy is conserved because the boundaries are insulated. In Table 3 the first three rows are for different orientations of

Table 3: Mean error in the cube over 4500 values from applying one calibration to several cases where the shape of the initially-heated region varies but its volume remains unchanged.

					(absolute)
L_1	W_1	H_1	T_{final}	SMAPE %	RMSE
0.50	0.25	1	0.125	4.68	0.0185
0.25	0.50	1	0.125	5.13	0.0218
1	0.50	0.25	0.125	6.66	0.0152
1	0.25	0.50	0.125	7.57	0.0266
1	1	0.125	0.125	8.04	0.0228
1	0.125	1	0.125	10.14	0.0423
0.125	1	1	0.125	11.02	0.0503

a heated region of size (1x1/2x1/4); for these cases the SMAPE error is less than 8 percent and the RMSE is less than 0.03. The last three rows of Table 3 are for different orientations of a flattened-out heated region of size (1x1x1/8); for these cases the SMAPE error is less than about 11 percent and the RMSE error is less than about 0.05. The results show that the error increases somewhat as the shape of the heated region diverges from the cube-shape used for calibration. However, the overall error values are acceptable for the rough level of precision needed to contribute to the AM application.

In a similar way the SG method was applied to bodies with varying-sized heated regions and to non-cubic bodies of fixed volume. The results of these additional studies (not shown to save space) provide error values comparable to those in Table 3. That is, calibration of the SG method on one body is a gateway to simulate a variety of heating geometries and body shapes.

4.4 Precision of the SG Method and Comparison with FEA

A detailed study is presented to provide evidence that the SG method gives physically meaningful results with acceptable precision. Several comparisons are presented in this section with the exact solution presented earlier. The comparison is carried out at several discrete locations along a corner-to-corner transit of the cube, and along a face-to-face transit of the cube, at locations shown in Figure 9. Figure 10 shows the comparison along the corner-to-corner transit. Figure 10a shows the temperature at three heated-region locations, and Fig. 10b shows the temperature at the three unheated-region locations. The temperature from the exact solution is also plotted. The best agreement is for the middle curve of Fig. 10a because this is the location used to fit the gain value. For every pair of curves (SG and exact), the curves begin at the same point, have the same shape, and are tending toward the same final temperature of $T/T_0 = 0.125$. Figure 10c shows the error value for all six locations plotted versus time.

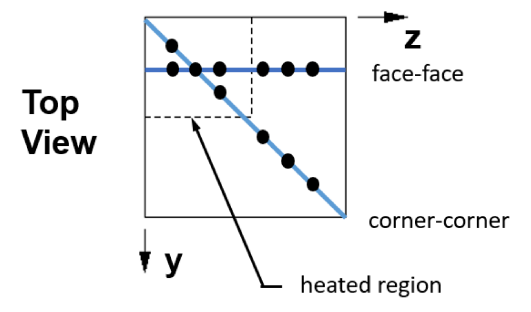


Figure 9: Six locations along a corner-to-corner transit of the cube (plots in Fig. 9) and six locations along a face-to-face transit of the cube (plots in Fig. 10) used for evaluating error in the calibrated SG method.

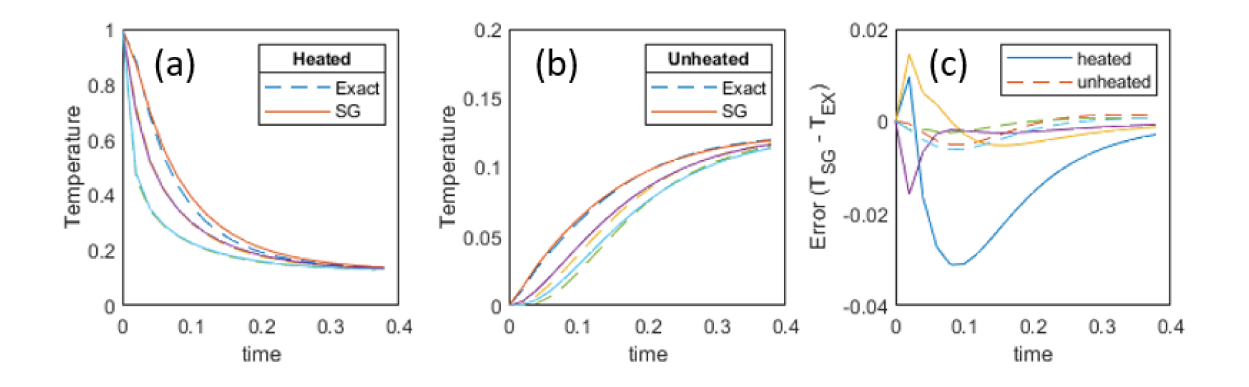


Figure 10: Temperature and error for six locations along a corner-to-corner transit of the cube (see Fig. 9 for locations) for the calibrated SG method, with $n_{tot} = 1536$ nodes and neighbor radius $\tilde{b} = 0.3$. (a) Temperature in the heated region (b) temperature in the unheated region (c) error for all six locations plotted versus time.

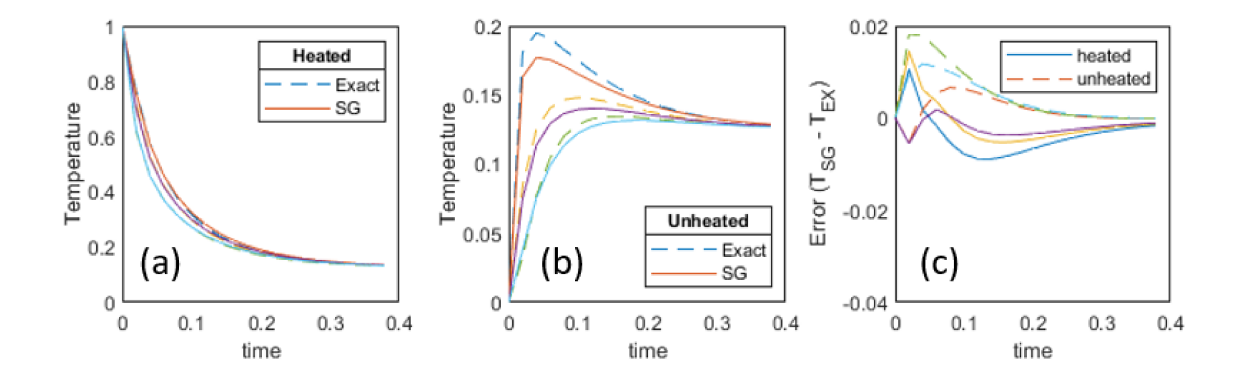


Figure 11: Temperature and error for six locations along a face-to-face transit of the cube (see Fig. 9 for locations) for the calibrated SG method, with $n_{tot} = 1536$ nodes and neighborhood radius $\tilde{b} = 0.3$. (a) Temperature at three locations in the heated region (b) temperature at three locations in the unheated region (c) error for all six locations plotted versus time.

Figure 11 shows the comparison along the face-to-face transit of the cube, again, at locations shown in Fig. 9. Figure 11a shows the normalized temperature at the three heated-region locations, and Fig. 11b shows the temperature at the three unheated-region locations. Note that the temperature in Fig. 11b for the unheated region first rises, then falls, because of the proximity to the heated region and in contrast to the shape of the temperature history along the diagonal shown in Fig. 10b. Figure 11c shows the time history of the error for the six points.

Table 4 shows error values, from comparison with the exact solution, for both the SG method and for results of a finite elment analysis (FEA) carried out with commercial software Abaqus. The error values are averaged over the time range time for each location, and the locations are taken from both the corner-to-corner transit and from the face-to-face transit. Two types of averaged error values are given, the symmetric mean absolute percentage error (SMAPE) defined in Eq. (36) and the root mean square error (RMSE) defined by

RMSE =
$$\left(\frac{1}{m} \sum_{i=1}^{m} [T_{ex}(t_i) - T_{sg}(t_i)]^2\right)^{1/2}$$
 (50)

For the SG method, carried out with 1536 nodes and with neighbor size $\tilde{b} = 0.3$, Table 4 shows the RMSE error is less than 0.018 everywhere and the SMAPE values are less than

10 pecent everywhere, with the largest value in the unheated region. The SMAPE values tend to be larger at locations farthest from the heated region. For the FEA analysis, carried out with 9261 nodes, the RMSE error is everywhere less than 0.017 and the SMAPE values are everywhere less than 12 percent. The largest SMAPE values for the FEA analysis also occur in the heated region. At many locations the FEA errors are larger than the SG errors, even though six times more nodes were used for the FEA analysis.

Table 4: Error for SG results and FEA results, by comparison with an exact solution, at several locations (refer to Fig. 8) in the partially heated cube. Both SMAPE and RMSE error are given which are averaged over the time range (0 < \tilde{t} < 0.4).

			Spectral Graph		FEA (ABAQUS)	
location		(1536 nodes)		(9261 nodes)		
X	У	\mathbf{Z}	SMAPE	RMSE	SMAPE	RMSE
0.15	0.15	0.15	2.7400	0.017850	2.3906	0.016919
0.25	0.25	0.25	0.8245	0.004877	2.0111	0.010396
0.35	0.35	0.35	0.6053	0.004325	1.7192	0.009505
0.65	0.65	0.65	1.1600	0.001259	5.4397	0.009440
0.75	0.75	0.75	6.0921	0.003235	8.7527	0.010892
0.85	0.85	0.85	10.0173	0.002599	11.7532	0.011756
0.25	0.25	0.15	1.1316	0.005843	2.1357	0.012168
0.25	0.25	0.25	0.8245	0.004877	2.0111	0.010396
0.25	0.25	0.35	0.5966	0.002651	1.8573	0.008136
0.25	0.25	0.65	1.5087	0.008071	1.4488	0.004348
0.25	0.25	0.75	1.6503	0.005840	2.0714	0.005192
0.25	0.25	0.85	1.3080	0.003402	5.6774	0.017143

5 Application to Additive Manufacturing

Additive manufacturing (AM) refers to a host of processes for which material is gradually added layer-upon-layer. The AM process allows creation of parts with complex geometries in a short time that are difficult or impossible to make with conventional subtractive or

formative manufacturing processes. However, poor part quality and process inconsistency presently restricts the wider applicability of the AM process. The thermal history of the part is a key determinant of its quality [16].

Accurate quantitative modeling approaches based on finite element (FE) analyses have been successfully developed and applied for understanding the thermal aspects of AM at the part-level as summarized in review papers [17, 18]. However, non-proprietary approaches are computationally expensive, with simulation of a few deposited layers amounting to many hours, if not days. For example, Cheng et al., reported that the computation time for thermomechanical analysis for a 6 mm cuboid shape exceeds 92 hours [19].

Hence, newer computationally efficient approaches are needed to approximate the temperature for different part designs and process parameters. In the context of FE-based modeling, it is important to note that certain commercial software, such as Autodesk Netfabb and Ansys 3DSim, have leveraged adaptive meshing to drastically reduce the computational time. However, the underlying mathematics of these commercial applications is proprietary [20, 21].

5.1 Advantages of the SG Approach for Thermal Modeling in AM

The computational advantages in using the spectral graph method to solve the heat conduction equation are two-fold.

1. Reduced computational burden due to elimination of mesh-based analysis.

Instead of solving the heat diffusion equation for each element through element birth-and-death techniques as in FE analysis, in the present paper the temperature in the part is associated with nodes of a planar graph projected onto the part geometry. Comparing results from the spectral graph approach with those of FE analysis shows that a significant portion of the computation effort in FE analysis is consumed by the meshing of elements, and simulation of the birth-and-death process to mimic material deposition in AM. The spectral graph approach greatly simplifies the meshing process, and as a result, the computation time for simulation of AM processes can be considerably reduced compared to existing, non-proprietary FE analysis-based approaches.

2. Reduced computational burden due to elimination of matrix inversion steps.

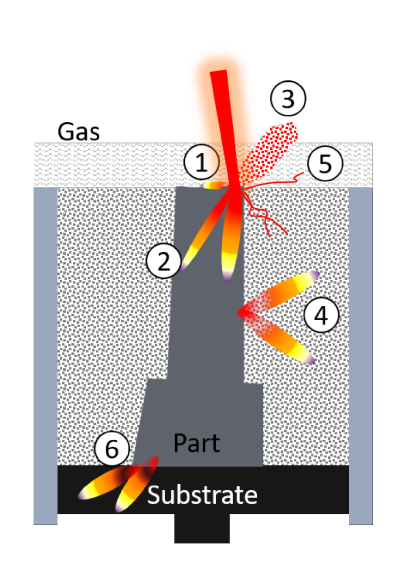
The SG method e required to solve the heat conduction equation. While FE analysis rests on matrix inversion for each timestep in the solution of the heat conduction equation, the spectral graph method instead relies on the more computationally tractable matrix multiplication operations to obtain the temperature, which greatly reduces the computational burden. Moreover, if the temperature is needed at a later time portion of an AM cycle, it may be computed directly in one large time step without computing the temperature at intermediate times and without loss of precision.

These advantages significantly reduces the computational time for predicting the temperature within the build time, compared to hours, if not days required by existing non-proprietary finite element simulations. The near real-time prediction of the temperature distribution in AM parts in turn enables the following developments.

- Physics-based, as opposed to expensive trial-and-error, optimization of the process parameters
- Feed-forward control of the AM process to preempt defects, as opposed to purely data-driven machine learning and analytics.
- Prediction of distortion and microstructural evolution.
- Identify red-flag problems in the part design and placement of supports.

5.2 Assumptions for Thermal Modeling of AM

In this paper a specific type of AM processs is considered, laser powder bed fusion (LPBF). In LPBF a layer of powdered metal is depositied on a build plate and selectively sintered by a laser. Then the build plate is lowered by one layer thickness (typically 50 micometers) and a new layer of powdered metal is deposited and sintered. Refer to Fig. 12 for a schematic of the LPBF process. The heat energy supplied by the laser (200 - 500 W) and the repeated melting/refreezing of the metal causes steep thermal gradients in the part, which are responsible for defects such as cracking and distortion [22]. In the LPBF process there is a short period of laser-scanning (and metal sintering) which is followed by a longer laser-off period for metal solidification, heat dissipation, and powder addition. Consequently the simulation of LPBF has two length scales and two time scales. First, the small-scale thermal details (less than 200 micrometers) are associated with the short-duration laser-sintering process (a few seconds), and second, the larger scale involving diffusion of heat throughout the yet-incomplete part during the longer laser-off portion (up to 60 s) of each cycle.



Laser Powder Bed Fusion

Salient Thermal Phenomena in LPBF.

- 1 Part-Energy Source Interaction Zone
 Latent Heat of Melting & Solidification.
 Meltpool Marangoni Convection
- 2 Part-Part Interaction Zone Conductive Heat Transfer
- Part-Gas Interaction Zone Radiative Heat Transfer
- 4 Part-Powder Interaction Zone Convective Heat Transfer
- Energy Source-Part-Powder Interaction Zone

 (5) Reflection, Absorption, Keyhole melting-effect
- 6 Part-Substrate Interaction Zone Conduction

Figure 12: Heat transfer phenomena present in the laser powder bed fusion (LPBF) process.

In the LPBF context, the following simplifying assumptions are applied to the spectral graph approach. The thermal properties of the material are static, in that, they do not change as the material changes state from particulate matter to a liquid (meltpool formation), and then back to a solid. In other words, the latent heat of melting and solidification is ignored. The heat loss due to vaporization, and material composition and density changes due to mass transfer are also not considered. Likewise, the radiative effects from the top surface of the part are not considered. The laser is considered a moving point heat source, i.e., the beam diameter and shape, and subsequent diffusion of the laser on the powder bed surface are not included. It is assumed that the laser energy is completely absorbed in the topmost layer and are not repeatedly reflected by the powder. Hence, variations in thermal absorptivity contingent on powder packing density are ignored [23].

For simplicity it is assumed that there is only one metal part on the build plate at a given time, hence there is no heat exchanged with other metal parts. The powder bed is considered to be at the same temperature as the chamber, and that the packing density of the powder bed remains static.

Lastly, temperature nodes belonging to the next layer are deposited on the previous printed layer to simulate deposition and fusion. Alternately, temperature nodes may be added in a subset of a layer called a hatch, if a finer resolution simulation of the fusion process is desired.

5.3 Simulation Parameters

A realistic part geometry was chosen for the LPBF process in order to compare the finite element (FE) method using Abaqus software and the new spectral graph approach. The test part has the shape of letter N which is shown in Figure 13. This test part has several

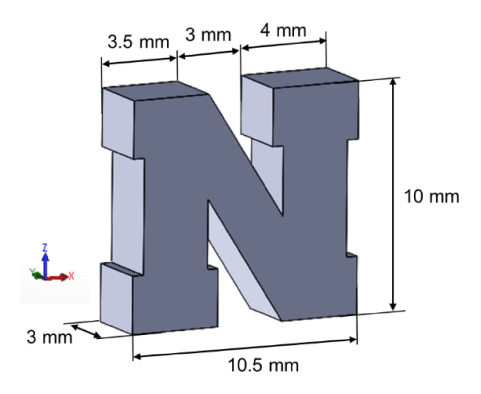


Figure 13: The geometry of the N-shaped part.

overhangs and undercuts that are challenging to sinter as they tend to collapse in the absence of anchoring supports [22]. Overhang regions also have reduced rates of heat removal owing to the poor thermal conductivity of the underlying powder, and to the reduced heat flow in the restricted cross section of the part, which is a key reason for poor build quality of overhang structures. The deposition strategy, process parameters, and material properties of this simulation study are reported in Table 5, which are similar to those in a previous paper in which the spectral graph approach was calibrated by comparison with FE method and with experimental temperature data [24]. Next a brief discussion is given of the convection heat-loss terms listed in Table 5. The convection coefficient to the build plate provides a heat sink to represent the thermal effect of the build plate without including a full simulation of heat conduction within the build base. The convection coefficient to the surrounding power is set to a small value $(10^{-5} \text{ W/m}^2/\text{K} \text{ which is functionally zero})$

Table 5: Simulation parameters for comparison between FE and spectral graph method.

Simulation Parameters	Values
Layer thickness (mm)	0.2 mm
Total number of nodes in the part, n	~ 3000
Node Density (nodes per mm ³)	~ 12
Number of neighbors connected to each node	50
Gain factor, g	1.3×10^4
Convection coefficient of powder, h_w (W m ⁻² K)	10^{-5}
Convection coefficient of build plate, h_s (W m ⁻² K)	10^{-2}
Ambient temperature, T_{∞} (K)	300
Inter-layer cooling time (s)	6.5
Material	SS 316
Density, ρ (kg m ⁻³)	8440
Thermal diffusivity, $\alpha \ (\mathrm{m^2 \ s^{-1}})$	3×10^{-6}

to agree with the insulated boundary (no heat loss) studied earlier in the paper. Although this insulated boundary with the powder somewhat simplifies the simulation, it is uniformly applied to both the SG method and to the FE method so as to maintain the validity of the comparison.

A summary of spectral graph simulation in metal additive manufacturing processes is illustrated schematically in Figure 14. The graph theory simulation studies require tuning of two types of factors:

- (1) Number of Nodes (n). Generally, if the part is discretized with a high number of nodes provides, the simulation error is smaller but at the cost of higher computation time. Hence, choosing the total number of nodes should be a balance between accuracy and computation time.
- (2) Heat Diffusion Parameters. In the spectral graph approach two model parameters must be determined, namely, the gain factor g, Eqn. (38), and the neighborhood radius over which nearby nodes are connected (for this calculation we used an alternate parameter, the number of neighbors connected to each node). These parameters govern the connectivity of the nodes and diffusion of the heat in the part. These parameters were taken from a previous

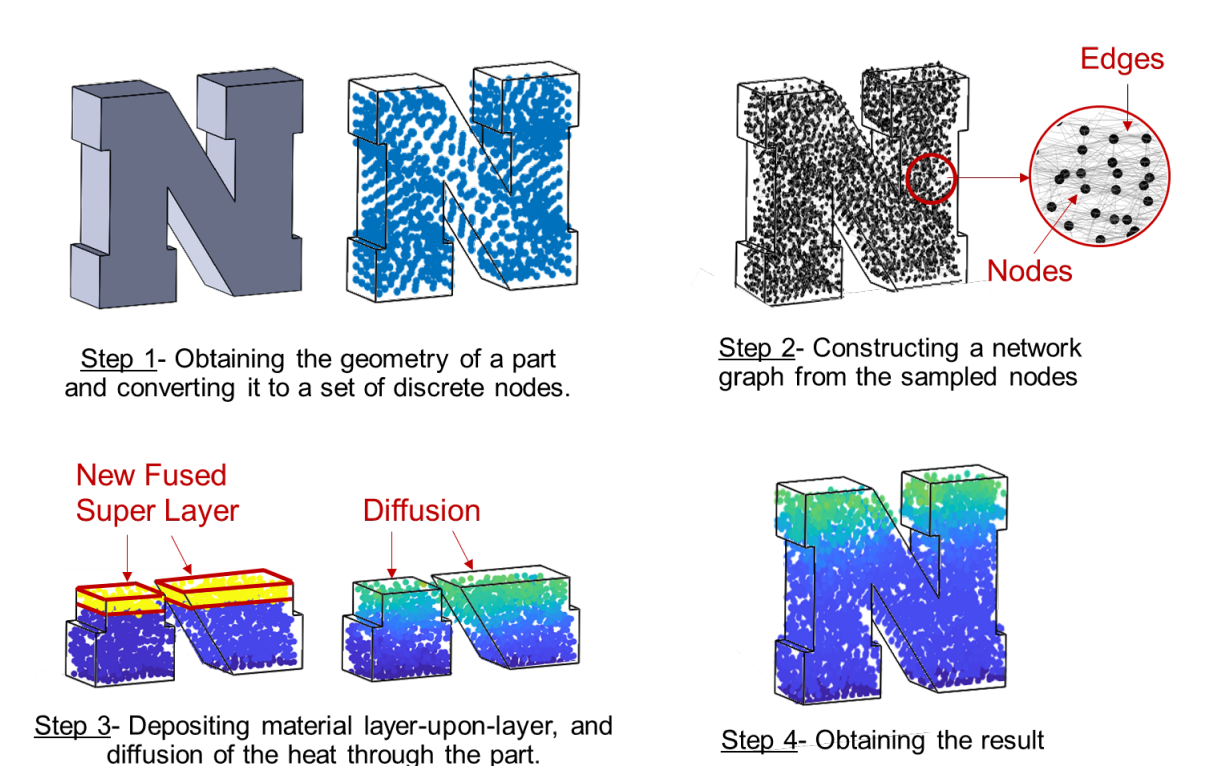


Figure 14: The four steps in the spectral graph simulation as applied to the N-shaped part

paper in which the SG method was calibrated with experimental thermal measurements [24].

For this study, two measurements points were selected on top surface of the N-shaped part, at left and right measurement points, as shown in Figure 15. To ensure an equitable comparison, about 3,000 nodes were used, with 0.2 mm layer thickness for deposition of stainless steel 316 for both the FEA and spectral graph approach.

5.4 Results of SG Thermal Modeling of AM

Figure 16(a) and Figure 16(b) show the predictions of the top surface temperature of the N-shaped part at left and right measurement points, respectively. There is a distinct kink or knee in each curve showing a change in the slope of the temperature history at layer 28; there is an increase is slope at left measurement point (Figure 16(a)) and a decrease in slope at the right measurement point (Figure 15(b)). This change in slope occurs when the left and right sections of the N-shaped part become connected to each other. The results

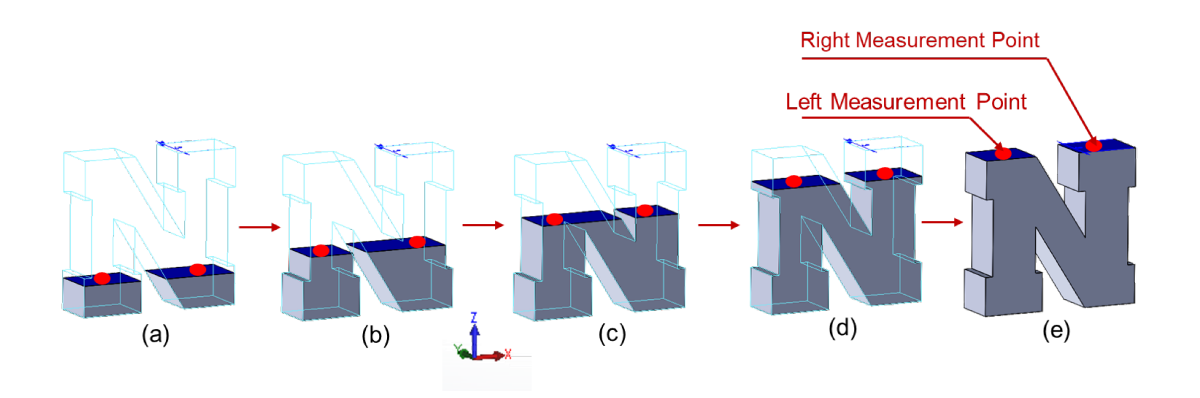


Figure 15: Positions of left and right measurement points at different layer height. (a) Layer 10, (b) Layer 20, (c) Layer 30, (d) Layer 40, and (e) Layer 50

are divided in two different phases:

Phase 1: This phase represents the beginning of the print (layer 1 to layer 28), where the left section and right section of the N-shaped part are not connected to each other (Figure 15(a) and (b)). In this phase there is no heat transfer between left and right sections of the N-shaped part. During this phase the temperature levels of the left and right measurement points are significantly different. The left temperature at the end of this phase is 450 K, while the right measurement point reaches temperature 550 K. The main reasons for the higher temperature on the right (100 K higher) are the bigger printing cross section (more laser heating) and overhang geometry (base-plate area for heat sink is smaller than heating area).

Phase 2: This phase includes of printing layer 28 to layer 50, after the left and right sections of the N-shaped part have become connected to each other. The temperature difference of left and right measurement points is only 50 K at the end of Phase 2 (layer 50) which is 50% lower than Phase 1.

In the spectral graph approach, the kink separating phase 1 and phase 2 occurs two layers earlier (layer 26) than FEA (layer 28) due to the nature of node connectivity of the approach. This kink at the connection layer is more gradual (both left and right measurement points) compared with sharp increase at FEA. The reason is that the distance-based meshing method of the SG method connects nodes across the small gap, slightly before the end of phase 1, if nodes are within the neighbor radius. This occurs two layers before the actual end of phase 1 when the two sections become connected. This effect can be seen

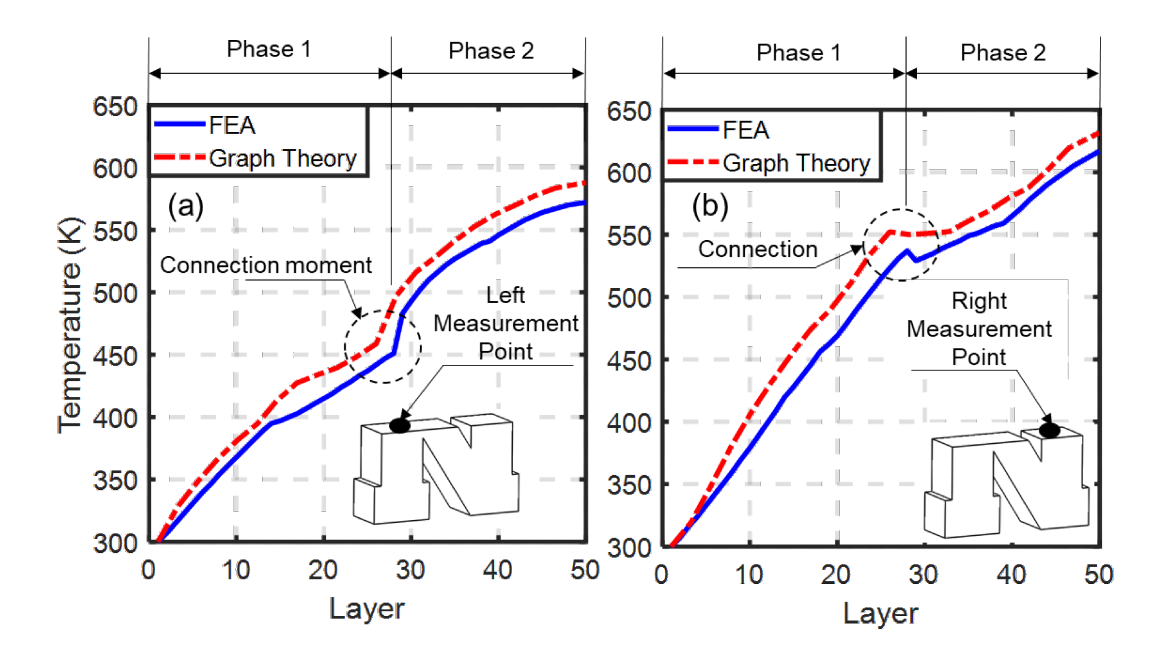


Figure 16: Comparison of top surface temperature of the FE and spectral graph approach for N-shaped part. (a) Top surface temperature at left measurement point. (b) Top surface temperature at right measurement point.

in Figure 17(b) which shows a time-stretched view of the temperature history of the left measurement point. A full discussion of the connectivity of nodes and characteristic length of the spectral graph approach is available in previous papers [24, 25, 26]. Figure 17(c) and Figure 17(d) show the N-shaped part temperature distribution before and after the connection left and right sections connection.

Despite the minor difference at the boundary between phase 1 and phase 2, the overall trend (curve shape) of the spectral graph and the FEA method are the same. The Mean Absolute Percentage Error (MAPE) and Root Mean Square Error (RMSE) between the two methods, are 7.47% and 28 K, respectively.

Table 6 reports the comparison between two methods, the computation time of the spectral graph approach was 887 seconds (14 min), while FEA required 1,968 seconds (32 min.). That is, the spectral graph approach predicts the surface temperature of the additive manufactured part 2.3 times faster than the FEA method within 7.5% MAPE error. It is important to note that the SG method was carried out with a research code that has not been optimized for speed and which runs under an interpreted computer language (Matlab).

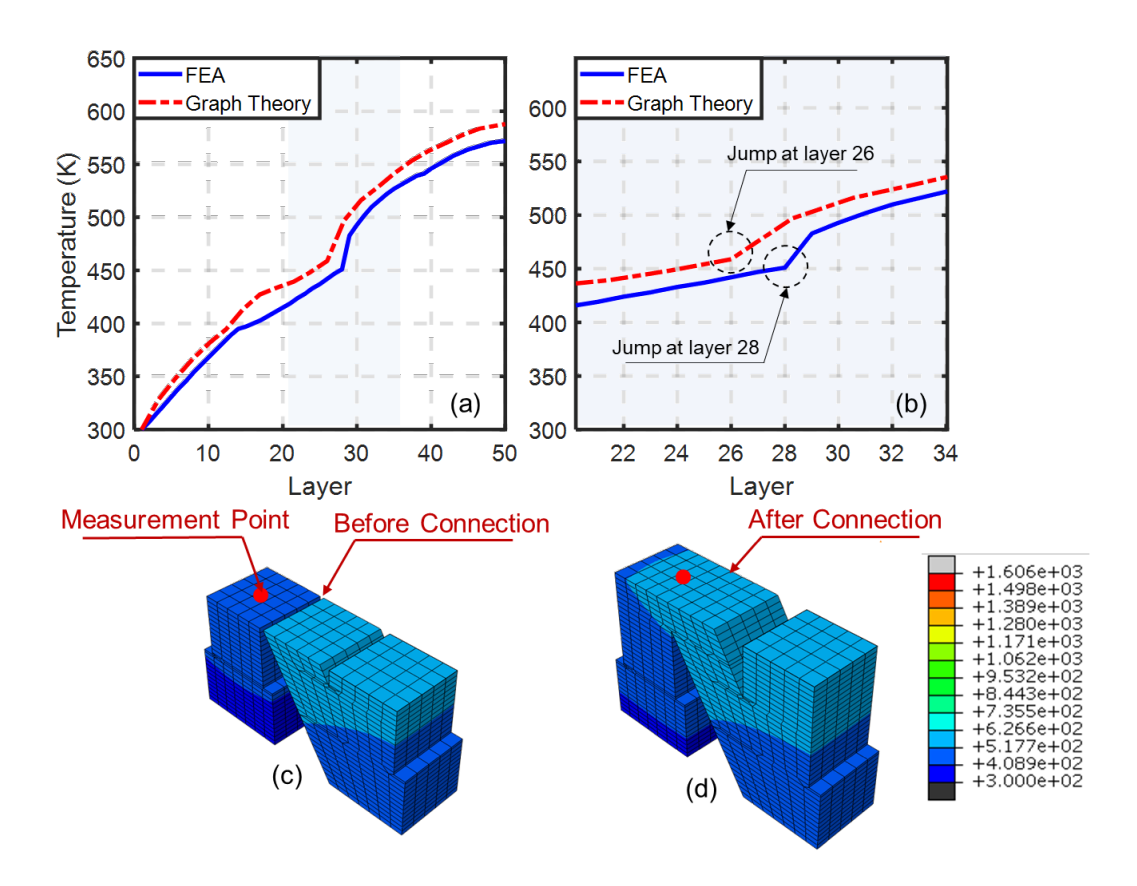


Figure 17: (a). Top surface temperature at the left measurement point. (b). Zoomed-in view of the left measurement point (c) Temperature distribution before the connection of the left and right sections (Phase 1). (d) Temperature distribution after the connection of the left and right sections (Phase 2).

Further increases in speed could be obtained by porting the SG algorithm to a compiled computer language (for example C++) and by applying multi-processor parallelization.

6 Summary and Future Work

Previous work by the authors showed that the SG approach has distinctive computational advantages in solving the heat conduction equation over the finite element method [26]. In the present work, the objective is to quantify the precision of the SG approach in the context of benchmark heat transfer problems for which exact analytical solutions are derived from

Table 6: Comparison of finite element (FE) method (Abaqus) and spectral graph (SG) method for N-shaped part using equal size layer thickness and equal number of nodes.

	Computation	MAPE	RMSE
	Time, s	%	(° K)
FE	1968 (32 min)	-	-
SG	887 (14 min)	7.5	27.7

first principles. The error in the SG solution is reported relative to the exact analytical solution for one—and three—dimensional bodies with planar boundaries. Solutions for these benchmark problems are also obtained with finite difference (one-dimensional body), and finite element (three-dimensional body) methods, and comparisons of computational speed with the SG approach are also given. Specific conclusions from these investigations are as follows:

- 1. For the one-dimensional problem, the relative error (symmetric mean absolute error) with the exact analytical solution ranges from 0.7 percent to 7 percent (coarse node distribution). The SG solution converges almost identically to the finite difference solution as the timesteps are decreased, and when a uniformly spaced node distribution is used.
- 2. For the three-dimensional problem, the precision of the SG method is explored for several heating conditions and several box-shaped bodies. The error associated with varying the heating condition is in the range of 3 to 11 percent. The three-dimensional cases also show the inter-relationship among the numerical parameters in the SG approach, and provides a systematic approach to calibrate these parameters against the exact analytical solution.
- 3. The error in the SG approach relative to the exact analytical solution for the three-dimensional cases were of the same order of magnitude as the finite element solution the worst case difference in error is 3 percent in favor of the SG method. Moreover, the SG approach requires less than 20 percent of the nodes of the finite element method; which provides a significant computational advantage for the SG approach.

4. A direct comparison was made between the SG method and a commercial finite element code applied to a 'N'-shaped body for a realistic simulation of an additive manufacturing process involving 50 layers of material. The SG method was computed 2.3 times faster with simulated temperature values within 7.5 percent of the FE code even though the SG code was run using an interpreted computer language (Matlab) without parallel processing, whereas the FE solver was implemented in an optimized commercial solver (Abaqus).

In future work, the SG approach will be further developed to: include type 1 and type 3 boundary conditions; include internal source terms; and, further increase the computation speed through use of a compiled computer language and through code parallelization.

Acknowledgement

The authors thank the National Science Foundation for grants OIA-1929172, CMMI-1719388, CMMI-1739696 and CMMI-1752069 (CAREER). The idea of using graph theory for thermal simulations in additive manufacturing was proposed and funded in CMMI-1752069. Supplemental funding through the NSF INTERN program for Reza Yavari to gain practical experience at Edison Welding Institute (EWI) is also appreciated.

References

- [1] Zhang, R., Hancock, E. R., 2008, "Graph Spectral Image Smoothing Using the Heat Kernel," Pattern Recognition, v. 41, pp. 3328-3342.
- [2] Ma, J., Huang, W., Segarra, S., Ribeiro, A., 2016, "Diffusion Filtering of Graph Signals and its Use in Recommended Systems," 41st Int. Conf. on Acoustics, Speech and Signal Processing, Shanghai, China, 20-25 March 2016, DOI: 10.1109/ICASSP.2016.7472541
- [3] Solomon, J., PDE Approaches to Graph Analysis, 2015, arXiv:1505.00185.
- [4] Belkin, M., Sun, J., and Wang, Y., 2008, "Discrete Laplace Operator on Meshed Surfaces," Proceedings of the Twenty-Fourth Annual Symposium on Computational Geometry, College Park, MD, June 911, pp. 278287.

- [5] Silling, S. A., and Askari, E., 2005, "A Meshfree Method Based on the Peridynamic Model of Solid Mechanics," Comput. Struct., 83(17), pp. 1526-1535.
- [6] Chen, Z., Niazi, S., Zhang, G., and Bobaru, F., 2017, "Peridynamic Functionally Graded and Porous Materials: Modeling Fracture and Damage," Handbook of Nonlocal Continuum Mechanics for Materials and Structures, G. Z. Voyiadjis, ed., Springer International Publishing, Cham, pp. 135.
- [7] Sun, Y.-S., and Li, B.-W., 2010, "Spectral Collocation Method for Transient Conduction-Radiation Heat Transfer," J. Thermophys. Heat Transf., 24(4), pp. 823832.
- [8] Rahmati, A. R., and Niazi, S., 2012, "Simulation of Microflows Using the Lattice Boltzmann Method on Nonuniform Meshes," Nanosci. Technol., 3(1), pp. 7797.
- [9] Xue, T., Tamma, K. K., Zhang, X., 2016, "A Consistent Moving Particle System Simulation Method: Applications to Parabolic/Hyperbolic Heat Conduction Type Problems," Int. J. Heat Mass Transfer, v. 101, pp. 365-372.
- [10] Ding, C., Cui, X., Deokar, R. R., Li, G., Cai, Y. Tamma, K. K., 2018, "An Isogeometric Independent Coefficients (IGA-IC) Reduced Order Method for Accurate and Efficient Transient Nonlinear Heat Conduction Analysis," Numerical Heat Transfer, Part A: Applications, 73:10, 667-684, DOI: 10.1080/10407782.2018.1470420.
- [11] Cole, K. D., Beck, J. V., Haji-Sheikh, A., and Litkouhi, B., Heat Conduction Using Green's Functions, 2nd edition, CRC Press, New York, 2011.
- [12] Carslaw, H. S., and Jaeger, J. C., 1959, Conduction of Heat in Solids, Oxford University Press, UK.
- [13] Patankar, S. V., 1980, Numerical Heat Transfer and Fluid Flow, Hemisphere Publishing Corporation, New York.
- [14] Cole, K. D., 2018, X22B00Y22B00Z22B00Tx5y5z5, "Parallelepiped with piecewise initial condition and insulated boundaries," Exact Analytical Conduction Toolbox, http://exact.unl.edu, accessed December 5, 2018.
- [15] Beck, J. V., 2003, "Sequential Methods in Parameter Estimation", Inverse Engineering Handbook, edited by K. A. Woodbury, CRC Press, New York.

- [16] Foteinopoulos, P., Papacharalampopoulos, A., and Stavropoulos, P., 2018, "On Thermal Modeling of Additive Manufacturing Processes," CIRP J. Manuf. Sci. Technol., v. 20, no. 1, pp. 6683.
- [17] Bandyopadhyay, A., and Traxel, K. D., 2018, "Invited Review Article: Metal-additive manufacturing-Modeling strategies for application-optimized designs," Additive Manufacturing, v. 22, pp 758-774.
- [18] Zhibo Luo, Yaoyao Zhao, 2018, "A Survey of Finite Element Analysis of Temperature and Thermal Stress Fields in Powder Bed Fusion Additive Manufacturing," Additive Manufacturing, Volume 21, 2018, Pages 318-332.
- [19] Cheng, B., Shrestha, S., and Chou, Y. K., 2016, "Stress and Deformation Evaluations of Scanning Strategy Effect in Selective Laser Melting," ASME 2016 11th International Manufacturing Science and Engineering Conference, pp. V003T008A009-V003T008A009.
- [20] Denlinger, E. R., Gouge, M., and Michaleris, P., 2018, Thermo-Mechanical Modeling of Additive Manufacturing, Butterworth-Heinemann.
- [21] Zeng, K., Pal, D., Gong, H. J., Patil, N., and Stucker, B., 2015, "Comparison of 3DSIM Thermal Modeling of Selective Laser Melting Using New Dynamic Meshing Method to ANSYS," Materials Science and Technology, 31(8), pp. 945-956. doi:10.1179/1743284714Y.0000000703
- [22] Sames, W.J., List, F. A., Pannala, S., Dehoff, R. R., and Babu, S. S. 2016, "The Metallurgy and Processing Science of Metal Additive Manufacturing," International Materials Reviews, 61:5, 315-360, DOI: 10.1080/09506608.2015.1116649
- [23] King, W. E., Anderson, A. T., Ferencz, R., Hodge, N., Kamath, C., Khairallah, S. A., and Rubenchik, A. M., 2015, "Laser Powder Bed Fusion Additive Manufacturing of Metals; Physics, Computational, and Materials Challenges," Applied Physics Reviews, 2(4), p. 041304.
- [24] Yavari, M. R., Williams, R. J., Hooper, P., Cole, K. D., and Rao, P. K., 2019, "Thermal Modeling in Metal Additive Manufacturing using Graph Theory: Experimental

- Validation with In-situ Infrared Thermography Data from Laser Powder Bed Fusion," accepted for publication, Journal of Manufacturing Science and Engineering.
- [25] Yavari, M. R., Cole, K. D., and Rao, P. K., 2019, "Design Rules for Additive Manufacturing Understanding the Fundamental Thermal Phenomena to Reduce Scrap," Procedia Manufacturing, 33, pp. 375-382 https://doi.org/10.1016/j.promfg.2019.04.046
- [26] Yavari, M. R., Cole, K. D., and Rao, P. K., 2019, "Thermal Modeling in Metal Additive Manufacturing Using Graph Theory," ASME Transactions, Journal of Manufacturing Science and Engineering, 141(7), pp. 071007-071027 10.1115/1.4043648